Article

Metal-Free g-C₃N₄/Nanodiamond Heterostructures for Enhanced Photocatalytic Pollutant Removal and Bacteria Photoinactivation

Natalya Kublik [1,2], **Luiz E. Gomes** [3], **Luiz F. Plaça** [1], **Thalita H. N. Lima** [4], **Thais F. Abelha** [4], **Julio A. P. Ferencz** [1], **Anderson R. L. Caires** [4] and **Heberton Wender** [1,*]

[1] Nano & Photon Research Group, Laboratory of Nanomaterials and Applied Nanotechnology (LNNA), Institute of Physics, Federal University of Mato Grosso do Sul, Campo Grande 79070-900, Brazil; natalyaemkublik@gmail.com (N.K.); luiz.placa@ufms.br (L.F.P.); julio.ferencz@ufms.br (J.A.P.F.)

[2] School of Manufacturing and System Networks, Ira A. Fulton Schools of Engineering, Arizona State University, Mesa, AZ 85212, USA

[3] Centro de Tecnologias Estratégicas do Nordeste (CETENE), Av. Prof. Luiz Freire, 01, Recife 50740-540, Brazil; luizedugo@gmail.com

[4] Optics and Photonics Group, Institute of Physics, Federal University of Mato Grosso do Sul, Campo Grande 79070-900, Brazil; thalita.lima212@gmail.com (T.H.N.L.); thaisbee@gmail.com (T.F.A.); anderson.caires@ufms.br (A.R.L.C.)

* Correspondence: heberton.wender@ufms.br

Abstract: Heterogeneous photocatalysis has emerged as a promising alternative for both micropollutant removal and bacterial inactivation under solar irradiation. Among a variety of photocatalysts explored in the literature, graphite carbon nitride (g-C₃N₄) is a metal-free semiconductor with acceptable chemical stability, low toxicity, and excellent cost-effectiveness. To minimize its high charge recombination rate and increase the photocatalyst adsorption capacity whilst keeping the metal-free photocatalyst system idea, we proposed the heterojunction formation of g-C₃N₄ with diamond nanocrystals (DNCs), also known as nanodiamonds. Samples containing different amounts of DNCs were assessed as photocatalysts for pollutant removal from water and as light-activated antibacterial agents against *Staphylococcus sureus*. The sample containing 28.3 wt.% of DNCs presented the best photocatalytic efficiency against methylene blue, removing 71% of the initial dye concentration after 120 min, with a pseudo-first-order kinetic and a constant rate of 0.0104 min⁻¹, which is nearly twice the value of pure g-C₃N₄ (0.0059 min⁻¹). The best metal-free photocatalyst was able to promote an enhanced reduction in bacterial growth under illumination, demonstrating its capability of photocatalytic inactivation of *Staphylococcus aureus*. The enhanced photocatalytic activity was discussed and attributed to (i) the increased adsorption capacity promoted by the presence of DNCs; (ii) the reduced charge recombination rate due to a type-II heterojunction formation; (iii) the enhanced light absorption effectiveness; and (iv) the better charge transfer resistance. These results show that g-C₃N₄/DNC are low-cost and metal-free photoactive catalysts for wastewater treatment and inactivation of bacteria.

Keywords: photodegradation; heterostructure; diamond nanocrystals; bacterial photoinactivation

1. Introduction

The conversion of solar energy into chemical energy using a semiconductor material has been extensively investigated to generate clean fuels and degradation of persistent organic pollutants (POPs) through environmentally friendly processes [1]. For efficient solar energy conversion, semiconductor photocatalysts are required to effectively absorb light in the visible range to achieve practical applications, present satisfactory stability under experimental conditions, and substantially possess suitable energy band positions and the ability to avoid photogenerated charge recombinations [2–4].

In a photocatalytic reaction, the conduction band (CB) and valence band (VB) energy position of the semiconducting photocatalyst must present more negative and more positive

values, respectively, compared to the reduction and oxidation potentials of the target molecules [4]. Examples include, but are not limited to, CO_2 reduction [5], H_2 and O_2 evolution by water splitting [3], and degradation of organic pollutants [6]. In the latter, in addition to the direct reduction or oxidation of the target molecules by the electrons and holes generated at the CB and BV, respectively, reactive oxygen species (ROS) such as superoxide anions ($O_2^{\bullet-}$) and hydroxyl radicals ($HO^\bullet$) are commonly involved in the pollutant removal and, in this case, the electron and hole potentials have to be suitable for their formation [4,7–9]. Additionally, some other relevant and desirable characteristics for a semiconductor material consist of low cost, recyclability, simple and scalable synthesis, and environmentally friendly composition [10,11].

Graphitic carbon nitride (g-C_3N_4) is a metal-free semiconductor that meets some of the above requirements since it presents good physicochemical stability and cost-effectiveness, negligible toxicity, and suitable CB energy as well as is easily prepared from a variety of precursors [12–14]. In regard to its energy band structure, g-C_3N_4 presents VB energies ranging from 1.40 to 1.59 eV (vs. NHE, at pH = 7), CB from -1.3 to -1.13 eV (vs. NHE, at pH = 7), and bandgap (E_g) energies of about 2.7 eV [15]. Its relative mild-gap provides only partial visible-light absorption, which along with its low separation efficiency of excited electron–hole pairs and deficient active sites, consists of the most relevant challenges concerning its optical activity [15]. These limitations, however, can be overcome by combining g-C_3N_4 with other suitable materials and thus fabricating heterojunctions [2,16–19].

Diamond nanocrystals (DNCs) are reported to have activation sites for both reduction and oxidation reactions, due to their high carrier mobility [20], as well as due to their potential intragap states caused by surface defects, unsaturated bonding, or impurities [21]. Based on its electronic properties, pristine DNC should not present significant photocatalytic activity under visible-light irradiation because of its high E_g value, of approximately 5.5 eV for bulk diamond and 3.3 eV for DNC powders [22], but the presence of impurities or defects may create donor or acceptor levels in its bandgap (intragap), facilitating the absorption of photons under visible-light irradiation conditions [23]. A coupling may occur between diamond and nondiamond C electrons in such a way that bandgap energies of less than 3.0 eV may be observed for the DNC [24]. The intragap states have been observed (but not commented on) in previous works [25], and treated as VB and CB of the DNC. However, DNC presents little to no cytotoxicity [26] and has been recognized as an outstanding material in photocatalysis along with graphene-based composites [24,27].

Relatively few works have applied DNC for photocatalytic degradation of pollutants [16,28,29], and even fewer have explored g-C_3N_4/DNC heterojunctions for wastewater purification and H_2 production [16,25,30]. Due to the various loose ends in the discussion on the chemical, physical, and photocatalytic properties of this system, further studies are highly desired. In the study carried out by Haleem et al. [30], 0.4 wt.% of DNC was added to g-C_3N_4 and the photocatalyst showed ~50% increased photocatalytic H_2 evolution compared to pristine g-C_3N_4, which was attributed to an enhanced charge transfer, low recombination rate, and higher surface area of the hybrid material. In a later work, the g-C_3N_4/DNC heterojunction prepared with 10 wt.% DNC showed the best photoactivity for H_2 evolution under visible-light irradiation [25]. In this case, the enhanced photoactivity was attributed to two factors: (i) the more localized charge carrier generation due to light-trapping from scattering properties of the DNCs, and (ii) the appropriated energy level matching of both materials to form a type-II heterojunction. Concerning a different preparation method and larger amounts of DNC in the heterojunction [16], a recent work evaluated the photocatalytic efficiency against the degradation of the methylene blue (MB) dye. The best photocatalytic degradation rate and dye adsorption capacity were observed in the sample containing 33 wt.% of DNC, which was associated with increased light absorption and greater surface area. Therefore, the g-C_3N_4/DNC is a metal-free composite material that has the potential to act as a photocatalyst in different photoactivated reactions.

Amongst the useful applications of g-C_3N_4 and DNC, their antibacterial capabilities have also been individually studied; a fact that is motivated by the urgent demand for

new materials capable of tackling pathogenic bacteria [31–33]. Under light illumination, g-C$_3$N$_4$ alone and in association with metals/semiconductors inactivated microorganisms through the generation of ROS [31]. Besides having photochemotherapy capabilities, g-C$_3$N$_4$ nanosheets also displayed cytotoxicity by inducing the rupture of the cell membrane of bacteria upon direct mechanical contact [34]. A similar physical mechanism of action is proposed for DNC-based antimicrobial agents [33]. These materials have gained increased biomedical interest due to their favorable biocompatibility; however, cytotoxicity against both Gram-positive and Gram-negative bacteria was displayed by modifying their surface composition [35]. Nanodiamonds could also inhibit biofilm formation and disrupt biofilms, which is particularly important considering that microorganism aggregates are harder to tackle than planktonic dispersions [36]. In addition, the combination of DNC with photosensitizers enabled the photodynamic antimicrobial chemotherapy against planktonic *S. aureus* [37,38] and its biofilms [37].

In this context, we prepared metal-free photocatalysts by making a heterojunction between g-C$_3$N$_4$ and as-obtained DNC under the in situ urea decomposition. The heterojunctions were prepared, characterized, and evaluated in terms of their photocatalytic activities for the photodegradation of MB and *Staphylococcus aureus* photoinactivation. The mechanism of improved photocatalytic efficiency under illumination was thoroughly revised, revealing it to be a combination of increased adsorption capacity, better light absorption effectiveness, enhanced charge transfer resistance, and decreased charge recombination rate by a type-II heterojunction formation. These results show that g-C$_3$N$_4$/DNC are efficient low-cost and metal-free photoactive catalysts for wastewater treatment and photoinactivation of bacteria.

2. Materials and Methods

2.1. Pristine Samples Preparation

The g-C$_3$N$_4$ samples were obtained through urea decomposition (Alphatec—São Paulo, Brazil, 99.9%) in an alumina crucible with a loose lid (see details in Figure S1, Supplementary Materials), according to previous reports with modifications [39,40]. After cooling naturally, the obtained content was macerated into a yellow powder and stored at room temperature. Non-detonated DNC samples were purchased from NaBond with a purity of 99.95% and used without further purification.

2.2. Synthesis of the g-C$_3$N$_4$/DNC Heterojunctions

For the heterostructures formation, a suitable amount of urea (Table S1) was solubilized in 25 mL of deionized water in a crucible with a loose lid for 15 min, under magnetic stirring. The amount of urea was calculated based on the mean yield of its conversion to g-C$_3$N$_4$ that in our experiments was 4.4%. Then, a certain mass of DNC (Table S1) was added to the mixture and sonicated (UltraCleaner 1400 A—model unique, 40 kHz—315 W RMS) for 30 min. For the DNC, the initial mass was calculated considering the rate of mass loss obtained at 550 °C by thermogravimetric analysis (TGA). The solution was dried at 120 °C for 6 h using a heating rate of 5 °C min^{-1}. Next, the crucible was heated at 550 °C for 2 h using a rate of 3 °C min^{-1} under an air atmosphere. The obtained porous powder was ground and stored for further analysis. The flowchart in Scheme 1 illustrates the described methodology. Samples were named as g-C$_3$N$_4$/DNC-2, g-C$_3$N$_4$/DNC-11, and g-C$_3$N$_4$/DNC-28, according to their approximated experimental DNC *w/w*%, respectively, found by TGA analysis (see TGA results) and considering their calculated synthesis yield of 3.0%, 2.3%, and 1.9%, respectively (Table S1).
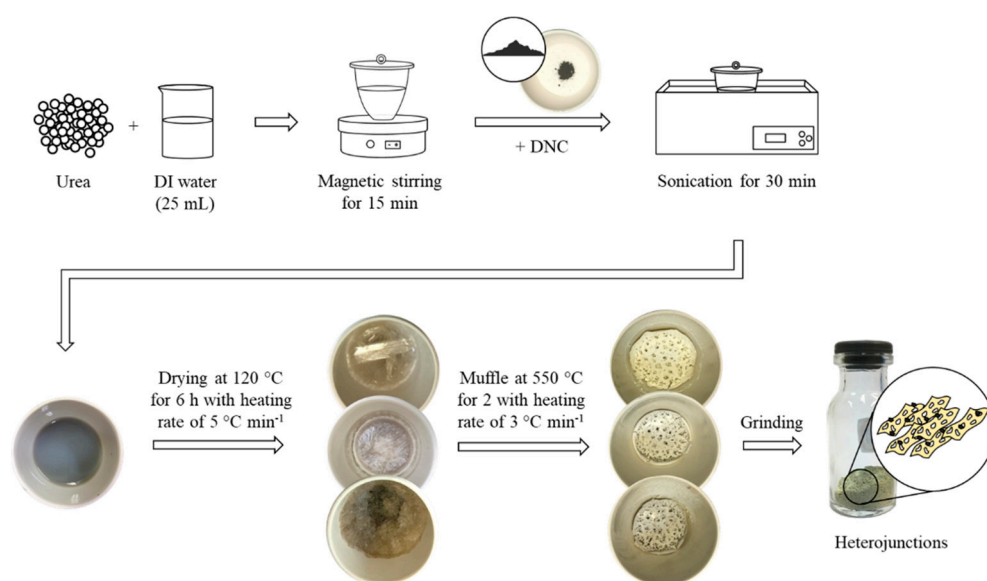
Scheme 1. The standard synthesis procedure of g-C$_3$N$_4$/DNC heterojunctions.

2.3. Characterization

Thermogravimetric (TGA) and differential scanning calorimetry (DSC) analysis were performed with a Netzsch STA 449 F3 Jupiter equipment under N$_2$ atmosphere, from 25 °C to 900 °C, with a 10 °C min^{-1} rate and 1 °C interval between measurements. The morphological features of the samples were observed by scanning electron microscopy (SEM) by using a JEOL JSM-6380 LV microscope and transmission electron microscopy (TEM) by using an FEI MORGANI 268 D operated at 80 kV. SEM measurements were performed by placing small amounts of the powder samples on the top of a carbon tape and TEM by dispersing the samples into isopropyl alcohol followed by deposition on carbon-coated Cu grids. Crystallinity was investigated by X-ray diffraction (XRD) using a Shimadzu XRD-6100 diffractometer. For the XRD analysis, the diffractometer was adjusted to 40.0 kV—30.0 mA, and 2θ scanning was in the 5°–85° range. Obtained diffractograms with Co-Kα X-ray source (λ_{Co} = 1.792850 Å) were adapted to typical Cu-Kα source typical conditions (λ_{Cu} = 1.544390 Å) to compare the peaks with the ones from the literature. Fourier transform infrared spectroscopy (FTIR) was carried out with an attenuated total reflection (ATR) accessory in a Perkin Elmer Spectrum 100 equipment. For dynamic light scattering (DLS) and Zeta potential (ZP) measurements (Malvern, Zetasizer Nano ZS), approximately 0.5 mg of each sample were sonicated in DI water for 10 min, and three measurements with 12 runs each were recorded at room temperature. Diffuse ultraviolet-visible reflectance spectroscopy (DRS-UV–Vis) with a Ø60 mm integrating sphere and Tauc plots was applied to determine the other optical bandgap. Brunauer−Emmett−Teller (BET) specific surface area measurements were examined by N$_2$ adsorption−desorption with an ASAP 2420 Micromeritics instrument. Steady-state photoluminescence (PL) studies were performed using an FS-2 fluorescence spectrometer (Scinco, Seoul, Korea) and data were collected at room temperature using right-angle geometry (90° excitation/emission geometry) and a quartz cuvette with four polished faces and a 10 mm optical path length. The PL spectra were obtained using a 150 W Xe-arc lamp as an excitation source; Czerny–Turner monochromators for selecting excitation and emission wavelengths; and an R928 photomultiplier for collecting the photoluminescence signal. PL emission spectra were obtained under excitation at 371 nm.

Electrochemical impedance spectroscopy (EIS) and Mott–Schottky (M–S) analysis were performed using a CorrTest potentiostat/galvanostat in a standard three-electrode electrochemical cell, with samples as the working electrode, Ag/AgCl as the reference electrode, and a platinum wire as the counter electrode, all immersed in a 0.1 M Na$_2$SO$_4$ electrolyte (pH 6). The photoelectrode preparation was carried out by sonicating 4 mg of the

as-prepared sample powders in 2 mL of H_2O and then drop-casting 200 μL of catalyst ink directly onto a limited area of 1 cm^{-2} of pre-cleaned fluorine-doped tin oxide (FTO) glass substrate. After drying, 20 μL of Nafion solution (0.3 wt.%) was dropped on the film surface and left to dry spontaneously. EIS measurements were conducted with frequencies varying from 40 mHz to 100 kHz, the amplitude of 10 mV, and applied potential set as 0 V vs. the open circuit potential (OCP), under dark conditions. The Mott–Schottky (M–S) analyses were carried out by ranging the applied potential from −0.2 to −1.2 V at 1000 and 2000 Hz. Potentials versus the Ag/AgCl reference electrode ($E_{Ag/AgCl}$) were converted to RHE (E_{RHE}) by using the Nernst equation, where $E_{RHE} = E_{Ag/AgCl} + (0.059 \times pH) + 0.197$ V.

2.4. Photocatalytic Degradation Study

The photocatalytic properties of the samples were investigated against the photodegradation of methylene blue (MB) dye as a cationic model molecule to simulate pollutants removal from water. For each experiment, 25 mg of the photocatalyst was added to 25 mL of MB solution (30 mg L^{-1}) and left under dark conditions for 40 min (20 min under sonication and 20 min under magnetic stirring) to achieve dye adsorption equilibrium. The photoreactor was a borosilicate beaker placed below an Abet-Tech solar simulator equipped with a 150 W Xe lamp. The photon flux was calibrated to 200 mW cm^{-2} using a reference cell, as described elsewhere [9,41]. Once under irradiation, the solution was kept under magnetic stirring and the concentration of the remaining MB was monitored through UV−Vis spectrophotometry at 664 nm [42] every 20 min up to 160 min. Adsorption of the MB dye was investigated by C/C_i curves, where C is the concentration of MB at the time "t" and C_i is the initial concentration of MB. The photocatalytic effect was accounted for by the C/C_0 curves, where C_0 is the concentration of MB when the light was turned on.

2.5. Photocatalytic Inactivation of Bacteria

The photocatalytic bactericidal effect was tested against a *Staphylococcus aureus* strain (ATCC 25923). The bacterial suspensions were prepared with 40 μL of the bacterial strain added to 4 mL of Müller−Hinton Broth and incubated at 37 °C for 24 h. The catalyst at 125 mg L^{-1} was dispersed in 2 mL of a physiological saline (0.9% NaCl) solution containing the bacterial inoculum at 1.5×10^8 CFU/mL. After that, the samples were shaken at 120 rpm for 60 min. After the incubation, the samples were separated into two groups: non-illuminated and illuminated. The illuminated samples were placed in a 96-well plate (250 μL/well) and submitted to visible-light irradiation provide by RGB light-emitting diodes (LEDs). The samples were illuminated at 18 mW cm^{-2} for 1 h. Then, a serial dilution was performed until 1:32 for both illuminated and non-illuminated samples. Finally, the colony-forming units (CFU) were counted after 24 h of incubation at 37 °C.

3. Results and Discussions

Metal-free photocatalysts are of great interest for solar energy conversion due to their low cost of production. Herein, we prepared heterojunction composites between g-C_3N_4 prepared from urea decomposition and as-obtained DNC through an in situ methodology. To obtain the experimental percentage of DNC in the g-C_3N_4/DNC heterostructures, as well as the thermostability of the composites, TGA experiments were carried out (Figure 1). Small weight losses (~2%) are observed from room temperature up to 200 °C for both the pristine g-C_3N_4 and g-C_3N_4/DNC composites which are attributed to desorption of physically adsorbed and intercalated water [43]. From 200 to 500 °C, it is clear that the samples presented almost negligible weight loss, and for higher temperatures, the decomposition of g-C_3N_4 could be evidenced, which was completed at around 770 °C, in agreement with previous reports [44]. For the DNCs, the residual mass observed was as high as 94.4% at 794 °C, similar to that obtained by Piña-Salazar et al. [45]. This small mass loss of the DNC refers to the release of gases adsorbed on its surface, such as CO, CO_2, and H_2O. Based on that, the temperature of 794 °C was used as a reference point for obtaining the residual masses (as indicated in the graph) and consequently the wt.% of DNC in the composites,

since at this temperature the residual mass percentage of the g-C$_3$N$_4$ is negligible. The amount (wt.%) of DNC in the photocatalysts was then estimated to be 1.6, 11.1, and 28.3% for samples g-C$_3$N$_4$/DNC-2, g-C$_3$N$_4$/DNC-11, and g-C$_3$N$_4$/DNC-28, respectively. This quantification considers the fact that the calculated synthesis yield decreased with respect to the increase in the initial DNC mass in the heterojunctions (Table S1). Therefore, there is a significant difference between the nominal amount of DNC introduced during the in situ synthesis and the experimentally obtained one, and this difference comes mainly from the reduced synthesis yield of g-C$_3$N$_4$ due to the presence of the DNC particles. To explain the synthesis yield decrease, we hypothesize that DNCs behaves as nanometer spots of heat transfer due to their highest thermal conductivity among existing materials [46], locally elevating the temperature of the surrounding intermediated products and accelerating the urea decomposition. As a result, the system ended with a lower content of g-C$_3$N$_4$ during the in situ heterojunction formation compared to the case without DNC. In addition, the DSC curve of the pristine g-C$_3$N$_4$ exhibited an endothermic peak centered at 720 °C, which shifted to 710 °C for the sample g-C$_3$N$_4$/DNC-28 (Figure S2 of the supplementary material). It shows that the g-C$_3$N$_4$ decomposition in the heterojunctions started and was accomplished earlier compared to the pristine g-C$_3$N$_4$. In addition, it is well-known that the yield of synthesis is strongly dependent on the temperature and time of reaction, and few increases in the temperature may result in a significantly reduced mass of g-C$_3$N$_4$ during the precursor decomposition [15]. To further validate our hypothesis, we prepared the heterojunctions by only physically mixing the DNC with the already prepared g-C$_3$N$_4$. The TGA results revealed a DNC experimental content remarkably close to the expected value (Figure S3), showing that in fact DNCs do not, in fact, cause direct decomposition of g-C$_3$N$_4$ but alters the kinetics and yield of urea decomposition to form the g-C$_3$N$_4$.
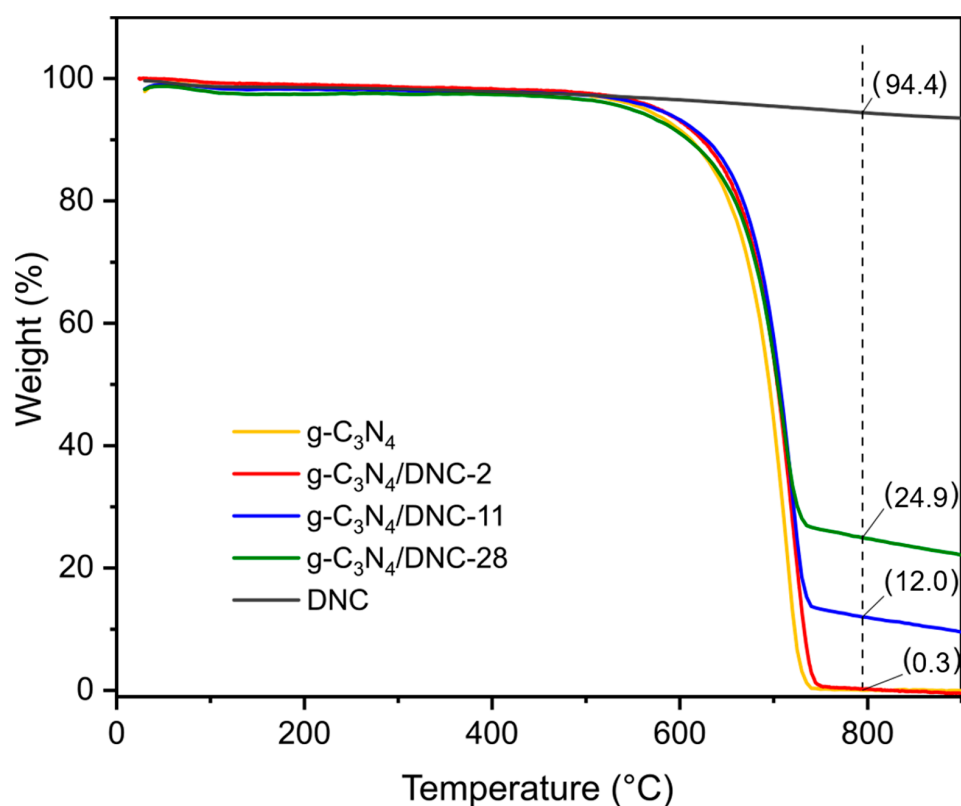

Figure 1. TG curves of pristine g-C$_3$N$_4$ and the g-C$_3$N$_4$/DNC heterojunctions.

Figure 2a,b, respectively, show a representative SEM and TEM image of the pure g-C$_3$N$_4$ sample that confirms that the morphology is composed of nanometer-thick sheets, as expected for a 2D material. Figure 2c shows the SEM image of the DNC sample, revealing

the formation of individual nanoparticles of about 100–200 nm, without formation of large aggregates. DLS results confirmed the formation of non-agglomerated particles in solution, with mean diameters of 125.4 ± 48.9 nm (see Figure S4). SEM and TEM analysis were also used to investigate the morphology of the g-C_3N_4/DNC heterojunctions (Figure 2d–h). As a result, g-C_3N_4 nanosheets functioned as supports for the DNC nanoparticles, preventing the formation of large crystal clusters and, consequently, enhancing the physical interaction between both materials. For the lower concentration of DNC (g-C_3N_4/DNC-2, Figure 2d), the sample morphology is like that of the g-C_3N_4 pristine sample, as expected. Additionally, a slight fragmentation of the g-C_3N_4 structure occurred when increasing the amount of DNC (Figure 2e,f). The representative TEM images of the g-C_3N_4/DNC-28 heterojunction confirm that DNC particles are dispersed and anchored over the nanosheet structures (Figure 2g–h).
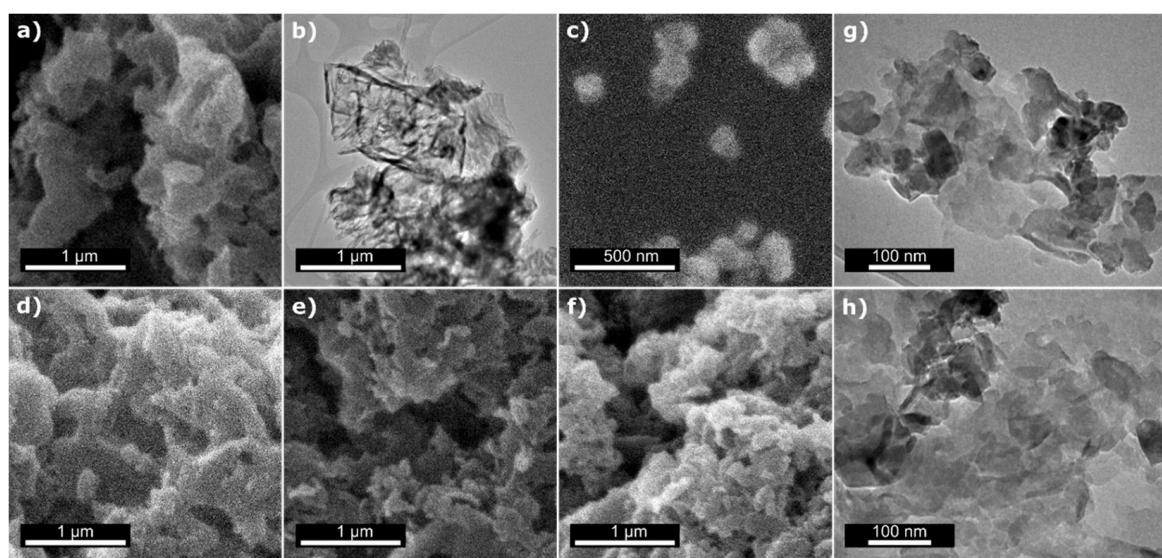

Figure 2. SEM (**a**) and TEM image (**b**) of the g-C_3N_4 photocatalyst. SEM images of the DNC pristine sample (**c**) and of the g-C_3N_4/DNC heterojunctions with (**d**) 1.6 wt.%, (**e**) 11.1 wt.%, and (**f**) 28.3 wt.% of DNC. Representative TEM images (**g**,**h**) of g-C_3N_4/DNC-28 heterojunctions.

Figure 3 shows the diffraction patterns of the pristine and heterojunctions samples. The XRD pattern of pristine g-C_3N_4 shows two peaks located at 12.8° and 27.4° that can be indexed as the (100) and (002) diffraction planes, respectively, of a graphite-like structure (JCPDS 87-1526). In addition, the latter corresponds to an interlayer distance of d = 0.326 nm, which matches the value commonly reported for graphite-like carbon nitride materials [47]. The former peak is, on the other hand, a signature of tri-*s*-triazine-based g-C_3N_4 formation [15,48]. For the DNC pristine sample, the XRD pattern contains one peak located at 44.3° that can be indexed as the (111) diffraction planes of diamond cubic structure (JCPDS 03-065-0537) [49]. The XRD patterns of the heterojunctions contain only the three peaks reported above, without a signal of secondary impurity phases. Additionally, with the increase in the concentration of DNC, there is an increase in the intensity of the diffraction peak located at 44.3° which is consistent with the expected higher concentration of DNC in the samples. A close look at the (002) planes of g-C_3N_4 reveals an angular shift of the diffraction peak from 27.5° to 27.9° for the heterojunctions which is a consequence of a decrease in the distances between the adjacent g-C_3N_4 layers [15]. Similar behavior has also been reported when the annealing of urea was conducted at different and increasing temperatures, from 450 to 600 °C, where an increase in the crystal stability of g-C_3N_4 was hypothesized [39]. This assumption is also supported also by the reduced full width at half maximum (FWHM) of the (002) peaks as the DNC was introduced, revealing that the g-C_3N_4 is more crystalline. Therefore, in agreement with TGA findings, the DNCs

increased the crystal stability of the g-C_3N_4 in the heterojunction by the in situ formation of tight-packed nanosheets during the decomposition of urea. This result also confirms the hypothesis of localized spots of heat transfer around the DNC that may decrease the amount of g-C_3N_4 by facilitating its decomposition at temperatures slightly higher than 550 °C.
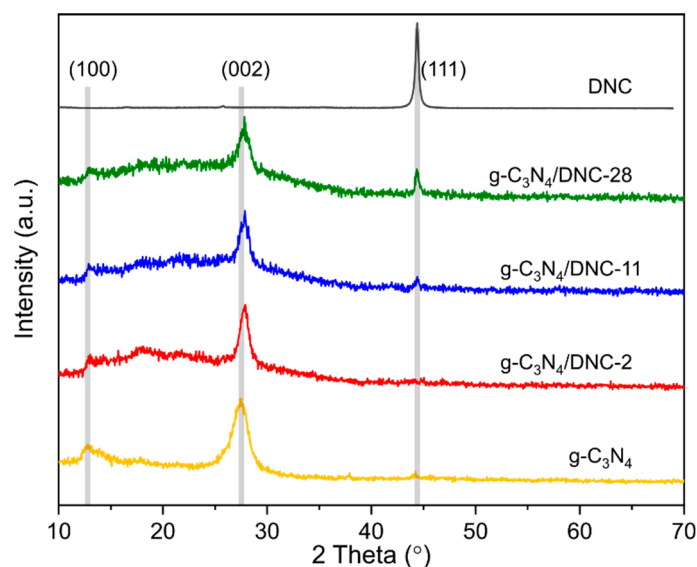

Figure 3. XRD patterns of pristine g-C_3N_4 and DNC, and the g-C_3N_4/DNC heterojunctions.

FTIR spectroscopy revealed chemical features of pristine DNC, g-C_3N_4, and the g-C_3N_4/DNC heterojunctions (Figure S5). It is possible to see that the spectra of pristine g-C_3N_4 and the heterojunctions are very similar and reflect the overall characteristics reported for g-C_3N_4 systems [15]. They show a sharp band at 810 cm^{-1} that is characteristic of this material and is attributed to the breathing mode of tri-*s*-triazine units [15,39]. The band at 890 cm^{-1} is ascribed to the out-of-plane C–H bond in aromatic domains [40] and, as also observed before, the spectra additionally present several strong bands in the 1200–1650 cm^{-1} region that are ascribed to the stretching mode of aromatic CN heterocycles [50]. These peaks together constitute a fingerprint of the g-C_3N_4 formation. Finally, the broadband observed between 3400 and 3000 cm^{-1} is ascribed to stretching vibrations of OH (3500–2500 cm^{-1}) and NH (3400–3300 cm^{-1}) groups, coming from water molecules physically adsorbed and/or the bridging C–NH–C units, respectively [15]. As expected, the pristine DNC presents less intense absorption bands since it contains fewer functional groups in both the bulk and surface chemical composition, showing a broad peak in the 3500–3000 cm^{-1} range, as observed for g-C_3N_4, as well as three main characteristic additional peaks at 1085, 1625, and 1707 cm^{-1}. The bands at 1085 and 1625 cm^{-1} can be attributed to the stretching vibration of C–O, and O–H, respectively. The broad band at 1700–1800 cm^{-1} is assigned to the C=O stretching vibration from the surface of DNC. It is also possible to observe that the DNC spectrum shows some minor features at 966, 915, and 810 cm^{-1} that together with the previously described peaks, are a fingerprint of the DNC. Therefore, the DNC surface contains functional groups that may help strengthen the physicochemical interaction with organic molecules or bacterial cells near the photocatalyst surface and enhance the overall composite photoactivity.

Figure 4a presents the UV−Vis−DRS curves of the samples. The g-C_3N_4 exhibited an optical reflectance edge at approximately 425 nm that corresponds to a direct bandgap of 2.91 eV (see Tauc plot in Figure 4b). Additionally, the increase in DNC concentration did not induce significant changes in the absorption edge (all samples presented bandgaps of ~2.9–3.0 eV) but resulted in an evident decrease in the total reflectance within the entire visible light range. This is a result of increased light absorption and/or light scattering effect caused by the addition of DNC. Su et al. observed similar results and mainly attributed

it to the effective light scattering of NDs [25]. However, it is noteworthy that as the DNC and g-C$_3$N$_4$ refractive indexes are, respectively ~2.4 and <1.5, the DNC would promote the incident light propagation through refraction, increasing its optical path at the junction interface [51,52] and, thus, the probability of photon absorption by the g-C$_3$N$_4$ in the heterojunctions. In fact, the optical properties of the DNC show thought-provoking aspects. The first is that two linear regions could be found in Tauc plots (Figure 4c), which represent two distinct bandgap energies of 2.64 and 4.83 eV. The latter is well-recognized for the bulk diamond structure and the former possibly comes from an intragap state due to (i) structural or surface defects or (ii) quantum confinement effects [23,53]. Therefore, the DNC studied herein, although to a lesser extent, may harvest visible light photons, especially considering electron jumps from its intragap energy level, and scattering is not a negligible factor.
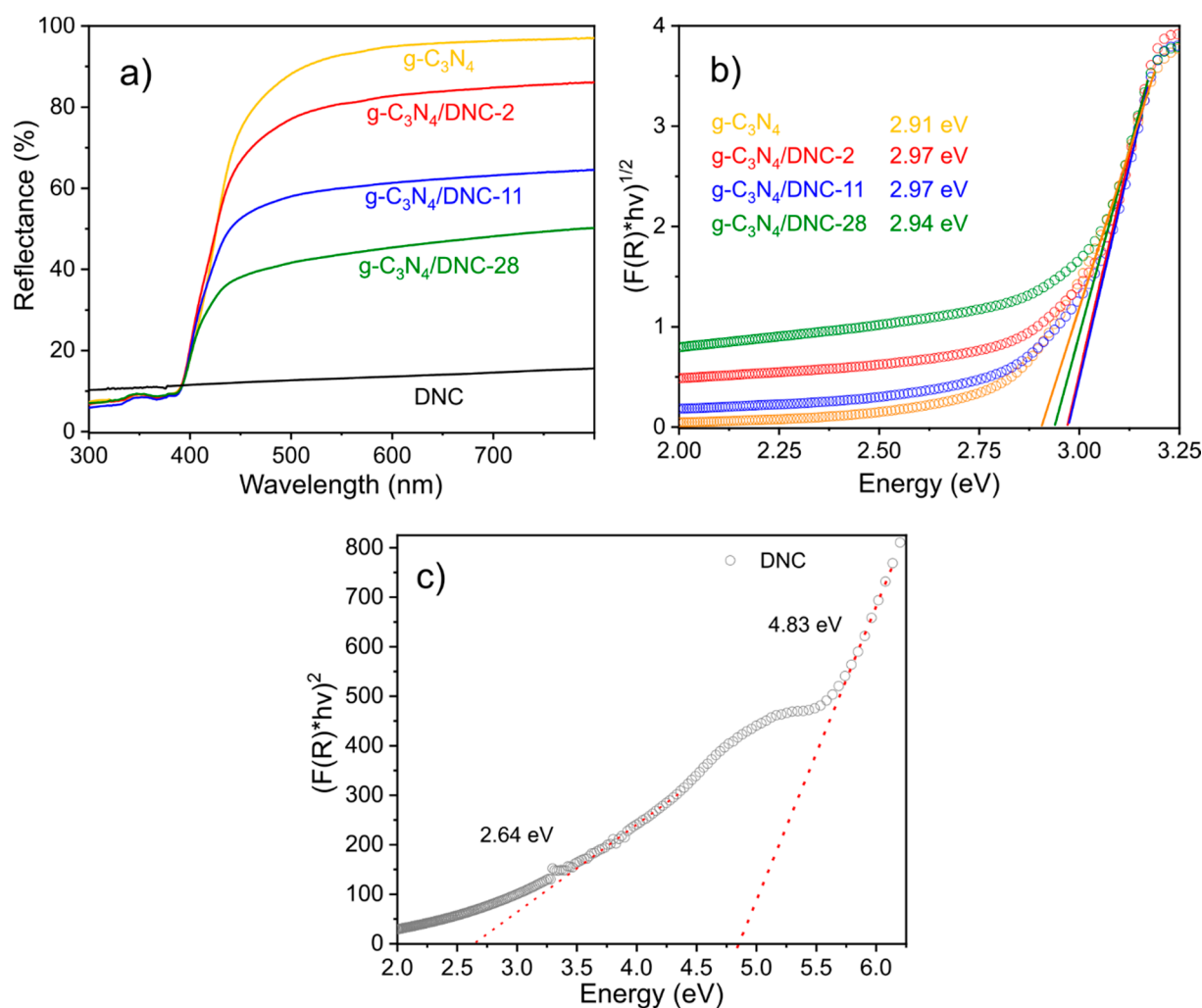

Figure 4. Diffuse reflectance spectra of pristine g-C$_3$N$_4$ and DNC, and the g-C$_3$N$_4$/DNC heterojunctions (**a**). Tauc plot for the indirect bang gap determination of pristine g-C$_3$N$_4$ and the prepared heterojunctions (**b**), and Tauc plot for the direct bang gap determination of the DNC (**c**).

To investigate the photocatalytic activity of the samples, experiments for photodegradation of the MB dye in water were conducted under simulated solar irradiation. Firstly, the MB dye adsorption efficiency without irradiation was studied for 40 min (Figure 5a), revealing that increasing DNC content enhances the adsorption efficiency of the MB in the photocatalysts, and pure DNC took a slightly longer time to achieve equilibrium in the dark (60 min, Figure S6). Similarly, the presence of DNC affected the zeta potential values, as the larger amount, the more electronegative were the heterojunctions: g-C$_3$N$_4$

(-17.2 mV), g-C$_3$N$_4$/DNC-2 (-15.5 mV), g-C$_3$N$_4$/DNC-11 (-18.2 mV), g-C$_3$N$_4$/DNC-28 (-27.6 mV), and DNC (-29.5 mV). The highly negative surface charge of the DNC favors the adsorption process through electrostatic interactions between cationic molecules and the negatively charged surface groups present in the photocatalysts. Specific surface area (S$_{BET}$) was determined according to the Brunauer–Emmett–Teller (BET) method using nitrogen adsorption isotherms, and the results show that the S$_{BET}$ values of the pristine DNC and g-C$_3$N$_4$ are 83.6 and 60.9 m^2 g^{-1}, respectively. All studied heterojunctions showed higher S$_{BET}$ values than the pristine materials but with values very close to each other, where g-C$_3$N$_4$/DNC-11 presented the largest surface area of 111.7 m^2 g^{-1}, followed by g-C$_3$N$_4$/DNC-28 (106.9 m^2 g^{-1}) and g-C$_3$N$_4$/DNC-2 (104.1 m^2 g^{-1}). Therefore, as it can be seen that the MB adsorption onto the photocatalysts does not follow the surface area trending perfectly. It is worth noting that the adsorption of the pollutant target molecule is an important but not the only step regarding its photocatalytic treatment. In this context, among the studied photocatalysts, the g-C$_3$N$_4$/DNC-28 showed a higher photoactivity for the removal of the MB under simulated solar irradiation at 200 mW cm^{-2} (Figure 5b). All photocatalytic results had a superior performance compared to the photolysis (the isolated light effect), showing that the photocatalyst material is crucial for MB degradation under light irradiation. The kinetic of the MB photocatalytic degradation follows a pseudo-first-order model with a constant rate of 0.0104 min^{-1} for the g-C$_3$N$_4$/DNC-28 sample, which is 76% higher than that obtained for pure g-C$_3$N$_4$ (0.0059 min^{-1}).
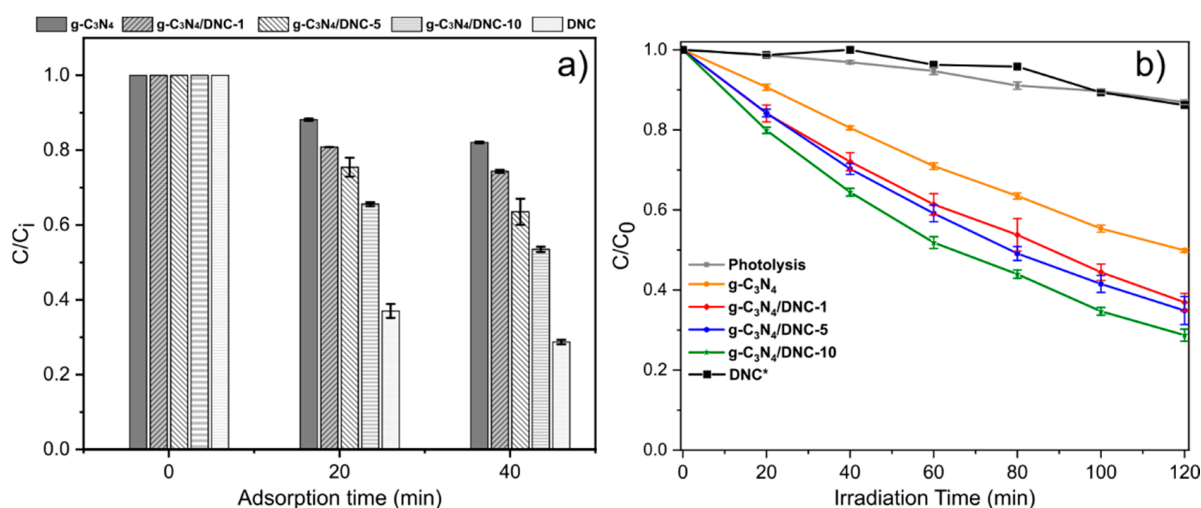

Figure 5. (**a**) C/C$_i$ bar curves for MB adsorption under dark conditions (20 min under sonication followed by 20 min under magnetic stirring) at initial [MB] = 30 mg L^{-1}, 1 mg mL^{-1} of photocatalyst, and 25 mL liquid volume. (**b**) Photocatalytic removal of MB dye in water using pristine g-C$_3$N$_4$ and DNC, and g-C$_3$N$_4$/DNC heterojunction samples under simulated solar illumination (AM1.5G filter) at 200 mW cm^{-2}. Note: Figure 5b was produced immediately after the adsorption step in the dark (40 min for all samples, except DNC* that presented the highest adsorption ability where 60 min under dark was necessary to establish equilibrium—Figure S6), and represents the concentration of MB at the time "t" divided by the concentration of MB at the moment the light was turned on (C$_0$). The MB concentration was not restored to 30 mg L^{-1} and error bars represent the mean standard deviation of the triplicate experiments.

As the produced heterojunctions showed efficient results for the photocatalytic degradation of MB, we studied their ability for the photoinactivation of a model bacterium. Figure S7 shows representative images of Petri dishes with photocatalyst-containing *Staphylococcus aureus* colonies grown under illumination and dark conditions. Exposure to the heterojunction composites photocatalyst in the dark or under light and without the photocatalysts (photolysis) did not impair the *Staphylococcus aureus* growth, Figure 6. On the other hand, g-C$_3$N$_4$ induced a significant reduction in bacterial growth under illumination, demonstrating its capability of photocatalytic inactivation of *Staphylococcus aureus*. In contrast, DNC did not promote the photocatalytic inactivation of bacteria under the

conditions explored herein, but the heterojunction containing 28 wt.% of DNC presented an improved photoinactivation capacity compared to the DNC-free sample (g-C$_3$N$_4$). This result may be due to the existing additional channel for oxidative radicals' production promoted by the heterojunction. Recent studies have demonstrated that g-C$_3$N$_4$ by itself can promote bacterial photocatalytic inactivation under visible-light illumination [14] and had its photoinactivation activity enhanced by preparing heterojunctions of g-C$_3$N$_4$ with different semiconductor nanomaterials [54,55].
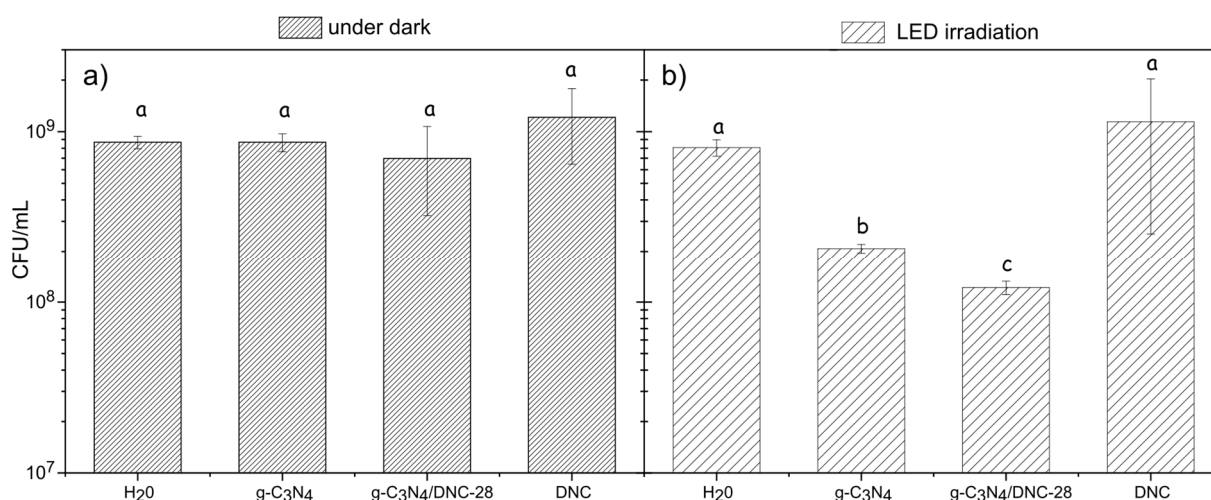
Figure 6. CFU mean values ($\pm$standard deviation) of *Staphylococcus aureus* when subjected to H$_2$O (negative control), and catalysts (g-C$_3$N$_4$, g-C$_3$N$_4$/DNC-28, and DNC) at 31 mg L^{-1} under dark (**a**) or LED irradiation (**b**). The duration of inactivation tests was 1 h and the irradiation source was RGB light-emitting diodes (LEDs) operated at 18 mW cm^{-2}. Means denoted by a different letter indicate significant differences between treatments ($p < 0.05$).

The photoluminescence (PL) technique can elucidate the role of DNC in the promotion or inhibition of e^-/h^+ recombination in g-C$_3$N$_4$. It is important to note that after photoexcitation of electrons to an excited state above or at the CB of a semiconductor, electron$-$hole pairs can recombine radiatively or non-radiatively, and these processes may occur through different routes with or without photon emissions, respectively [56]. Electron$-$hole recombination only contributes to PL band edge emission when photons are emitted with energies near the semiconductor bandgap, whilst nonradiative decays normally involve charge trapping at defect states within the bandgap [56,57]. This latter process involves the successful relaxation of charge carriers to the shallow surface trap states and the bottom of the CB$-$top of the VB in the case of holes. One should note that further radiative recombination coming from these trapped charges (donor$-$acceptor levels) may produce additional emission bands of lower energy than the band edge emission and may represent signs of intragap states in semiconductor materials. In addition, the intensity of emitted photons depends on the type/structure of materials [58] and the rate of e^-/h^+ recombination, where a lower PL emission intensity (at a fixed wavelength near the absorption band edge) may be indicative of lesser e^-/h^+ recombination [9,41,59,60]. Figure 7a presents the PL emission spectra obtained under excitation at 371 nm (excitation spectrum of pristine g-C$_3$N$_4$ is available in Figure S8) of the pristine g-C$_3$N$_4$ and the heterojunction samples. All samples show a broad PL emission that could be satisfactorily decomposed on three main Gaussian peaks (Figure 7b) centered at 438 nm (sigma $\approx$ 20), 466 nm (sigma $\approx$ 47), and 505 nm (sigma $\approx$ 47) which results from the recombination of e^-/h^+ from different pathways in g-C$_3$N$_4$ [30,61]. According to previous reports [62,63], these recombination paths come from the sp^3 C–N σ band, sp^2 C–N π band, and the lone pair (LP) state of the bridge N atom transitions, respectively, as depicted in the inset of Figure 7b. Additionally, the pure DNC did not show PL signal under these conditions, and as the amount of DNC increased, the overall PL intensity of the heterojunction was

lowered, indicating that photogenerated electrons in the excited g-C$_3$N$_4$ are transferred to the DNC immediately after the photo-production, reducing, therefore, the recombination rate of charge carriers, as also reported before [25,29,30,61].
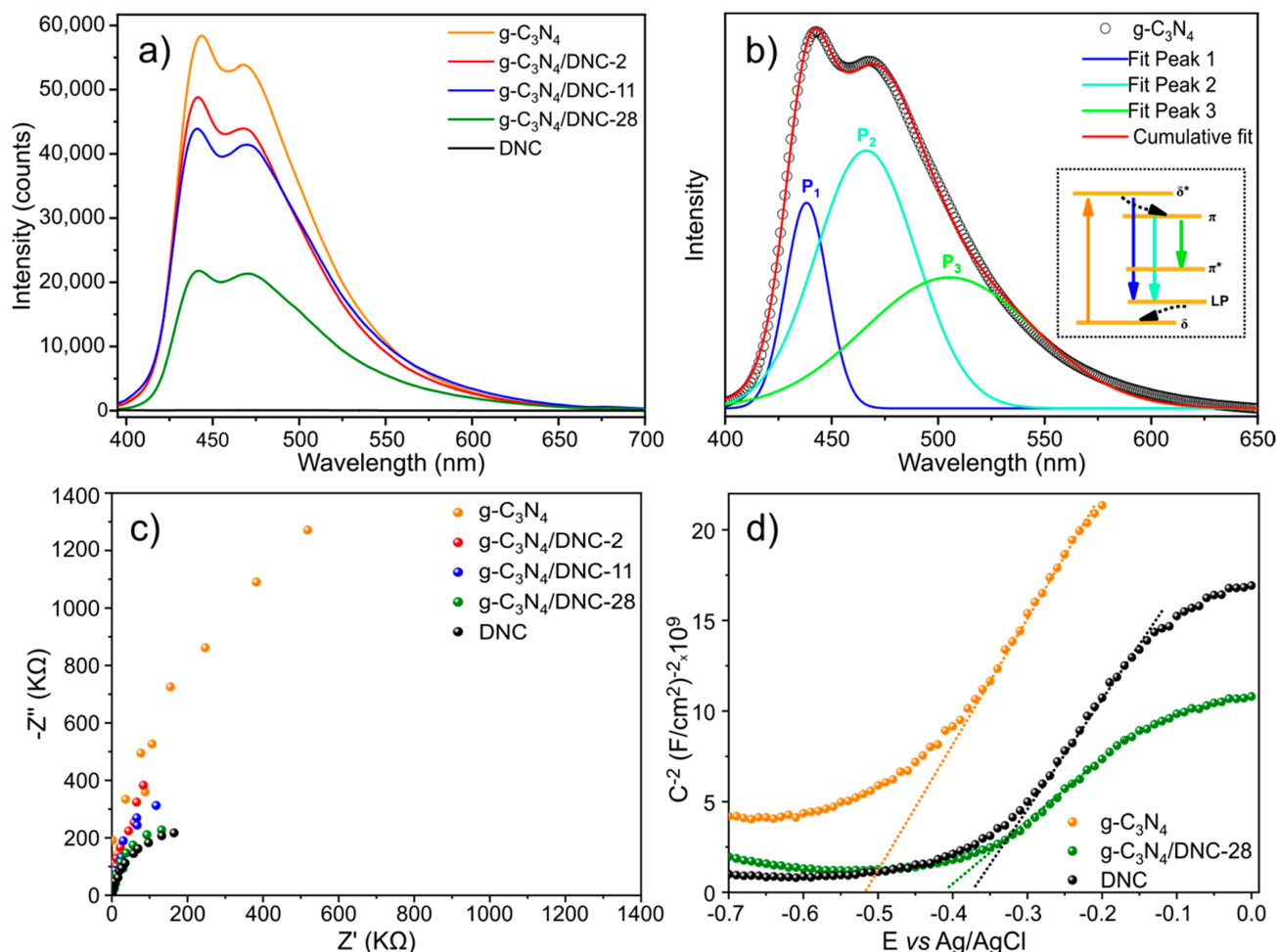

Figure 7. PL emission spectra under excitation at 371 nm (**a**); Gaussian peak fitting of g-C$_3$N$_4$ PL emission spectrum (**b**); EIS spectra under simulated solar light irradiation (**c**); and Mott−Schottky curves under dark conditions at 1000 Hz (**d**).

To further understand the charge transfer properties of the heterojunctions we performed EIS as a tool to study the charge transfer resistance at the interface formed between the semiconductor and the electrolyte and, indirectly, the separation of e^-/h^+ pairs at the electrode surface by monitoring the radii of the formed semicircles in the Nyquist plot (Figure 7c). It is known that the smaller the radius of the semicircle, the lower the resistance of charge transfer [64,65]. The EIS data showed a single semicircular arch for all the samples, and the radius of the semicircle diminished with the introduction of DNC in the compositions, thus indicating a lower charge transfer resistance when the diamond nanoparticles are present in the photoelectrode. Therefore, the EIS results corroborate the PL findings, indicating that DNC is working as an efficient cocatalyst on the surface of the g-C$_3$N$_4$, decreasing the recombination of the photogenerated charges and, consequently, improving the photocatalytic activity, as seen in the MB photodegradation and photoinactivation of *Staphylococcus aureus* bacteria.

For a better understanding of the photoactivity activity including the electronic properties of the photocatalysts, we conducted Mott–Schottky (M–S) analysis to determine the type of conductivity and the flab band potential (V_{fb}) of both pristine g-C$_3$N$_4$ and DNC, which is close to the CB in the case of n-type semiconductors. The M–S analysis consists of plotting $1/C^2$ against V, where C is the space charge layer capacitance, and V is the

applied voltage [66]. The V_{fb} of the electrode material can be obtained through the curve intercept at the horizontal axis, Figure 7d. The M–S plots of pristine and the heterojunction samples showed positive slopes, demonstrating that the photocatalysts present n-type conductivity and electrons are the majority charge carriers. The V_{fb} of the electrodes is ~-0.52 and -0.36 V (vs. Ag/AgCl) for both pristine g-C_3N_4 and DNC, respectively, and changed to an intermediate value of -0.42 V (vs. Ag/AgCl) for the heterojunction with 10% wt. of DNC. As the V_{fb} of n-type semiconductor materials lies very close to their CB minimum (~0.1–0.2 eV) [66], we can assume CB minimum positions of g-C_3N_4 and DNC at -0.17 and -0.01 V (vs. RHE), respectively. Therefore, by using the bandgap values of the individual semiconductors, their respective VB maximum values could be estimated as 2.73 and 4.82 V (vs. RHE), and the band position alignment of the heterojunction is proposed as illustrated in Figure 8.
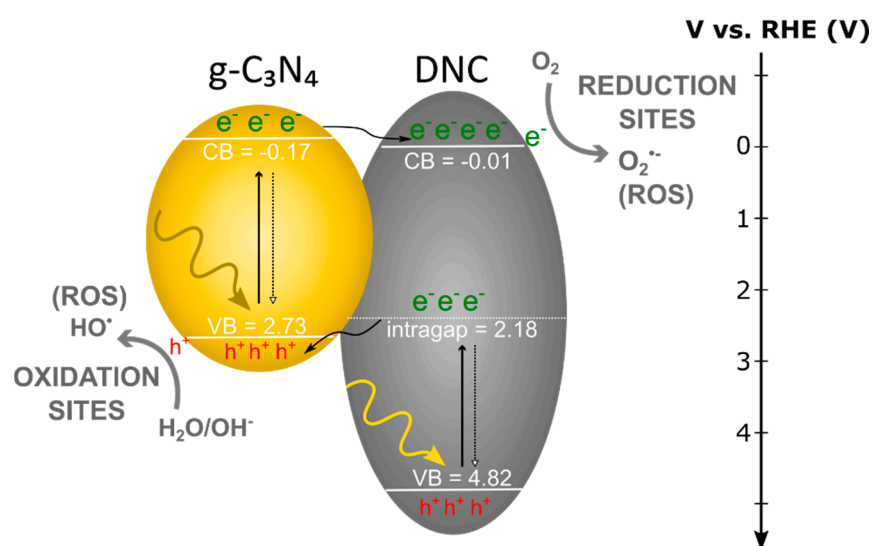

Figure 8. Mechanism of charge transfer and ROS formation in the g-C_3N_4/DNC nanosheets/NPs heterojunction.

The improved photoactivity of a heterojunction may come from the better separation of photogenerated charges and increased light absorption due to the dual-absorber semiconductor configuration [4,8]. Since more photons are absorbed, more free charges become available in the CB and VB of semiconductor materials. Depending on their electronic configurations, the photogenerated charges can physically separate, with electrons migrating to one of the semiconductors, and the holes to the other [4]. In this case, the recombination of electrons and holes decreases due to the created physical barrier, increasing the probability of redox reactions to occurs on the surface of the photocatalyst. On one hand, the photogenerated holes can drive direct oxidation reactions or react with H_2O or OH^- to produce hydroxyl radical hydroxyl, and on the other hand, the photogenerated electrons can drive direct reduction reactions or react with oxygen to form superoxide radicals.

In our case, a type-II g-C_3N_4/DNC heterojunction formed, in such a way that after photoexcitation of electrons to the CB of g-C_3N_4, those that did not straight recombine with the holes at the VB of g-C_3N_4 straight away could migrate to the CB of DNC due to its more positive potential. This latter surface works as an electron sink and triggers reduction reactions to directly attack the targeting adsorbed molecules or to generate superoxide radicals (Figure 8). On the other hand, after photoexcitation of electrons to the intragap states of DNC, they can recombine back to the VB of DNC or migrate to the VB of g-C_3N_4 due to its more negative potential, and recombine with holes present therein. However, it is important to note that the photoexcitation of DNC is not as efficient as for g-C_3N_4 under simulated solar light or LED irradiation and, therefore, the photoholes in the latter material are not completely consumed by recombination with electrons coming from the

DNC intragap states. Therefore, the oxidation reactions can still occur at the surface of the g-C$_3$N$_4$, with the reduction counterpart reactions happening at the DNC surface.

Therefore, the enhanced photocatalytic activity of the g-C$_3$N$_4$/DNC nanosheets heterojunction is a combination of some important factors. The first ones are the increased adsorption capacity of targeting molecules and enhanced light absorption effectiveness promoted by the presence of DNC. This is due to DNC's large surface area, available surface functional groups, and intragap states formation. Secondly, but no less important, is the decreased charge recombination rates due to the type-II heterojunction formation. Finally, the in situ formation of tight-packed g-C$_3$N$_4$ nanosheets during the decomposition of urea in the presence of DNC, correlated with the higher electrical conductivity of the latter, may facilitate charge transfer at the semiconductor/water interface. These results show that g-C$_3$N$_4$/DNC are efficient low-cost and metal-free photoactive catalysts for wastewater treatment and photoinactivation of bacteria.

4. Conclusions

This work demonstrated an effective and simple methodology to prepare type-II g-C$_3$N$_4$/DNC heterojunctions by adding DNC into urea decomposition in situ. Their structural, morphological, optical, and electronic properties were investigated in detail and the materials were applied as photocatalysts for the degradation of MB and photoinactivation of *Staphylococcus aureus*. The morphology of pure g-C$_3$N$_4$ was composed of nanometer-thick sheets, whilst DNC formed individual nanoparticles with a mean diameter of 125.4 ± 48.9 nm. Under the g-C$_3$N$_4$/DNC heterojunctions formation, the g-C$_3$N$_4$ nanosheets were slightly fragmented and functioned as supports for the DNC nanoparticles. The pristine g-C$_3$N$_4$ exhibited a direct bandgap of 2.91 eV and the DNC showed two distinct bandgap energies of 4.83 and 2.64 eV, the latter being a signal of intragap states due to structural/surface defects and/or quantum confinement effects. The obtained g-C$_3$N$_4$/DNC nanocomposite heterojunctions exhibited enhanced photocatalytic activity against MB degradation and *Staphylococcus aureus* inactivation under simulated solar light and LED irradiation, respectively. Due to its negative surface charge, the DNC enhanced the adsorption efficiency of the targeting molecules onto the photocatalyst by favoring electrostatic interactions between the cationic molecules and their negatively charged surface groups. The MB photocatalytic degradation followed a pseudo-first-order kinetic and the best photocatalyst (28 wt.% of DNC) showed a 76% higher degradation constant than pure g-C$_3$N$_4$. This sample also presented the highest *Staphylococcus aureus* photoinactivation activity. As the amount of DNC increased in the heterojunctions, the overall PL intensity was lowered, and the charge transfer resistance at the semiconductor/electrolyte interface followed an inverse trend, decreasing with increasing DNC concentration. This indicates that photogenerated electrons in the excited g-C$_3$N$_4$ are physically separated from the holes by transferring to the DNC nanoparticles immediately after photoexcitation, resulting in a reduced recombination rate of charge carriers. Both the g-C$_3$N$_4$ and DNC showed n-type semiconducting features and the mechanism of the decreased charge recombination was evidenced by a type-II heterojunction formation, with reduction and oxidation reactions occurring at the DNC and g-C$_3$N$_4$ surfaces, respectively. Overall, the improved photoactivity of the heterojunctions was due to better separation of photogenerated charges, increased light absorption, enhanced adsorption, and decreased charge transfer resistance. These results suggest that g-C$_3$N$_4$/DNC are efficient low-cost and metal-free photoactive catalysts for wastewater treatment and bacterial photoinactivation.

Supplementary Materials: The following are available online at https://www.mdpi.com/article/10.3390/photochem1020019/s1. Flowchart of g-C$_3$N$_4$ synthesis (Figure S1); DSC of g-C$_3$N$_4$ and g-C$_3$N$_4$/DNC-28 (Figure S2); TGA profiles for yield comparisons (Figure S3); DLS of the pristine DNC (Figure S4); Normalized FTIR spectra of pristine and prepared heterojunctions (Figure S5); Adsorption of MB under dark using the diamond nanocrystals (Figure S6); Growth of Staphylococcus aureus colonies in Petri dishes (Figure S7); Excitation PL spectrum of pristine g-C$_3$N$_4$ for emission fixed at 443 nm (Figure S8); Nominal content of DNC (wt%), masses used of both precursors in

the synthesis, and the obtained experimental DNC content (Table S1); and Kinect constant (k) and R-squared values for first-order MB photodegradation reaction using prepared samples (Table S2).

References

1. Li, M.; Liu, Y.; Dong, L.; Shen, C.; Li, F.; Huang, M.; Ma, C.; Yang, B.; An, X.; Sand, W. Recent advances on photocatalytic fuel cell for environmental applications—The marriage of photocatalysis and fuel cells. *Sci. Total Environ.* **2019**, *668*, 966–978. [CrossRef] [PubMed]

2. Masih, D.; Ma, Y.; Rohani, S. Graphitic C_3N_4 based noble-metal-free photocatalyst systems: A review. *Appl. Catal. B Environ.* **2017**, *206*, 556–588. [CrossRef]

3. Du, H.; Liu, Y.-N.; Shen, C.-C.; Xu, A.-W. Nanoheterostructured photocatalysts for improving photocatalytic hydrogen production. *Chin. J. Catal.* **2017**, *38*, 1295–1306. [CrossRef]

4. Stelo, F.; Kublik, N.; Ullah, S.; Wender, H. Recent advances in Bi_2MoO_6 based Z-scheme heterojunctions for photocatalytic degradation of pollutants. *J. Alloys Compd.* **2020**, *829*, 154591. [CrossRef]

5. Ye, S.; Wang, R.; Wu, M.-Z.; Yuan, Y.-P. A review on g-C_3N_4 for photocatalytic water splitting and CO_2 reduction. *Appl. Surf. Sci.* **2015**, *358*, 15–27. [CrossRef]

6. Navarro, R.M.; Alvarez-Galvan, M.C.; de la Mano, J.A.V.; Al-Zahrani, S.; Fierro, J.L.G. A framework for visible-light water splitting. *Energy Environ. Sci.* **2010**, *3*, 1865–1882. [CrossRef]

7. Feil, A.F.; Wender, H.; Gonçalves, R.V. Photovoltaic, Photocatalytic Application, and water Splitting. *Nanocatal. Ion. Liq.* **2016**, 275–294. [CrossRef]

8. Gonçalves, R.V.; Wender, H.; Khan, S.; Melo, M.A. Photocatalytic Water Splitting by Suspended Semiconductor Particles. *Nanoenergy* **2017**, 107–140. [CrossRef]

9. Nogueira, A.C.; Gomes, L.E.; Ferencz, J.A.P.; Rodrigues, J.E.F.S.; Gonçalves, R.V.; Wender, H. Improved Visible Light Photoactivity of $CuBi_2O_4$/CuO Heterojunctions for Photodegradation of Methylene Blue and Metronidazole. *J. Phys. Chem. C* **2019**, *123*, 25680–25690. [CrossRef]

10. Homem, V.; Santos, L. Degradation and removal methods of antibiotics from aqueous matrices—A review. *J. Environ. Manag.* **2011**, *92*, 2304–2347. [CrossRef]

11. Julkapli, N.M.; Bagheri, S.; Hamid, S.B.A. Recent Advances in Heterogeneous Photocatalytic Decolorization of Synthetic Dyes. *Sci. World J.* **2014**, *2014*, 692307. [CrossRef] [PubMed]

12. Sagara, N.; Kamimura, S.; Tsubota, T.; Ohno, T. Photoelectrochemical CO_2 reduction by a p-type boron-doped g-C_3N_4 electrode under visible light. *Appl. Catal. B Environ.* **2016**, *192*, 193–198. [CrossRef]

13. Mao, J.; Peng, T.; Zhang, X.; Li, K.; Ye, L.; Zan, L. Effect of graphitic carbon nitride microstructures on the activity and selectivity of photocatalytic CO2 reduction under visible light. *Catal. Sci. Technol.* **2013**, *3*, 1253–1260. [CrossRef]

14. Zhao, H.; Yu, H.; Quan, X.; Chen, S.; Zhang, Y.; Zhao, H.; Wang, H. Fabrication of atomic single layer graphitic-C_3N_4 and its high performance of photocatalytic disinfection under visible light irradiation. *Appl. Catal. B Environ.* **2014**, *152-153*, 46–50. [CrossRef]

15. Wen, J.; Xie, J.; Chen, X.; Li, X. A review on g-C_3N_4—Based photocatalysts. *Appl. Surf. Sci.* **2017**, *391*, 72–123. [CrossRef]

16. Zhou, L.; Zhang, H.; Guo, X.; Sun, H.; Liu, S.; Tade, M.; Wang, S. Metal-free hybrids of graphitic carbon nitride and nanodiamonds for photoelectrochemical and photocatalytic applications. *J. Colloid Interface Sci.* **2017**, *493*, 275–280. [CrossRef]

17. Silva, G.S.T.; Carvalho, K.T.G.; Lopes, O.; Ribeiro, C. g-C$_3$N$_4$/Nb$_2$O$_5$ heterostructures tailored by sonochemical synthesis: Enhanced photocatalytic performance in oxidation of emerging pollutants driven by visible radiation. *Appl. Catal. B Environ.* **2017**, *216*, 70–79. [CrossRef]

18. Yilmaz, E.; Soylak, M. Facile and green solvothermal synthesis of palladium nanoparticle-nanodiamond-graphene oxide material with improved bifunctional catalytic properties. *J. Iran. Chem. Soc.* **2017**, *14*, 2503–2512. [CrossRef]

19. Tian, Y.; Ge, L.; Wang, K.; Chai, Y. Synthesis of novel MoS$_2$/g-C$_3$N$_4$ heterojunction photocatalysts with enhanced hydrogen evolution activity. *Mater. Charact.* **2014**, *87*, 70–73. [CrossRef]

20. Isberg, J.; Hammersberg, J.; Johansson, E.; Wikström, T.; Twitchen, D.J.; Whitehead, A.J.; Coe, S.E.; Scarsbrook, G.A. High Carrier Mobility in Single-Crystal Plasma-Deposited Diamond. *Science* **2002**, *297*, 1670–1672. [CrossRef]

21. Holt, K.B. Undoped diamond nanoparticles: Origins of surface redox chemistry. *Phys. Chem. Chem. Phys.* **2010**, *12*, 2048–2058. [CrossRef]

22. Hirai, H.; Terauchi, M.; Tanaka, M.; Kondo, K. Estimating band gap of amorphous diamond and nanocrystalline diamond powder by electron energy loss spectroscopy. *Diam. Relat. Mater.* **1999**, *8*, 1703–1706. [CrossRef]

23. Choudhury, S.; Kiendl, B.; Ren, J.; Gao, F.; Knittel, P.; Nebel, C.; Venerosy, A.; Girard, H.; Arnault, J.-C.; Krueger, A.; et al. Combining nanostructuration with boron doping to alter sub band gap acceptor states in diamond materials. *J. Mater. Chem. A* **2018**, *6*, 16645–16654. [CrossRef]

24. Lin, Z.; Xiao, J.; Li, L.; Liu, P.; Wang, C.; Yang, G. Nanodiamond-Embedded p-Type Copper(I) Oxide Nanocrystals for Broad-Spectrum Photocatalytic Hydrogen Evolution. *Adv. Energy Mater.* **2015**, *6*. [CrossRef]

25. Su, L.-X.; Huang, Q.-Z.; Lou, Q.; Liu, Z.-Y.; Sun, J.-L.; Zhang, Z.-T.; Qin, S.-R.; Li, X.; Zang, J.-H.; Dong, L.; et al. Effective light scattering and charge separation in nanodiamond@g-C$_3$N$_4$ for enhanced visible-light hydrogen evolution. *Carbon* **2018**, *139*, 164–171. [CrossRef]

26. Yu, S.-J.; Kang, M.-W.; Chang, H.-C.; Chen, K.-M.; Yu, Y.-C. Bright Fluorescent Nanodiamonds: No Photobleaching and Low Cytotoxicity. *J. Am. Chem. Soc.* **2005**, *127*, 17604–17605. [CrossRef] [PubMed]

27. Pastrana-Martínez, L.M.; Morales-Torres, S.; Carabineiro, S.A.C.; Buijnsters, J.; Faria, J.; Figueiredo, J.; Silva, A.M.T. Nanodiamond-TiO$_2$Composites for Heterogeneous Photocatalysis. *ChemPlusChem* **2013**, *78*, 801–807. [CrossRef] [PubMed]

28. Kim, K.-D.; Dey, N.K.; Seo, H.O.; Kim, Y.D.; Lim, D.C.; Lee, M. Photocatalytic decomposition of toluene by nanodiamond-supported TiO$_2$ prepared using atomic layer deposition. *Appl. Catal. A Gen.* **2011**, *408*, 148–155. [CrossRef]

29. Sampaio, M.J.; Pastrana-Martínez, L.M.; Silva, A.M.T.; Buijnsters, J.G.; Han, C.; Silva, C.G.; Carabineiro, S.A.C.; Dionysiou, D.D.; Faria, J. Nanodiamond–TiO$_2$ composites for photocatalytic degradation of microcystin-LA in aqueous solutions under simulated solar light. *RSC Adv.* **2015**, *5*, 58363–58370. [CrossRef]

30. Haleem, Y.A.; He, Q.; Liu, D.; Wang, C.; Xu, W.; Gan, W.; Zhou, Y.; Wu, C.; Ding, Y.; Song, L. Facile synthesis of mesoporous detonation nanodiamond-modified layers of graphitic carbon nitride as photocatalysts for the hydrogen evolution reaction. *RSC Adv.* **2017**, *7*, 15390–15396. [CrossRef]

31. Zhang, C.; Li, Y.; Shuai, D.; Shen, Y.; Xiong, W.; Wang, L. Graphitic carbon nitride (g-C$_3$N$_4$)-based photocatalysts for water disinfection and microbial control: A review. *Chemosphere* **2018**, *214*, 462–479. [CrossRef] [PubMed]

32. Norouzi, N.; Ong, Y.; Damle, V.G.; Najafi, M.B.H.; Schirhagl, R. Effect of medium and aggregation on antibacterial activity of nanodiamonds. *Mater. Sci. Eng. C* **2020**, *112*, 110930. [CrossRef] [PubMed]

33. Wang, C.; Makvandi, P.; Zare, E.N.; Tay, F.R.; Niu, L. Advances in Antimicrobial Organic and Inorganic Nanocompounds in Biomedicine. *Adv. Ther.* **2020**, *3*. [CrossRef]

34. Cui, H.; Gu, Z.; Chen, X.; Lin, L.; Wang, Z.; Dai, X.; Yang, Z.; Liu, L.; Zhou, R.; Dong, M. Stimulating antibacterial activities of graphitic carbon nitride nanosheets with plasma treatment. *Nanoscale* **2019**, *11*, 18416–18425. [CrossRef]

35. Wehling, J.; Dringen, R.; Zare, R.N.; Maas, M.; Rezwan, K. Bactericidal Activity of Partially Oxidized Nanodiamonds. *ACS Nano* **2014**, *8*, 6475–6483. [CrossRef] [PubMed]

36. Zhang, T.; Kalimuthu, S.; Rajasekar, V.; Xu, F.; Yiu, Y.C.; Hui, T.K.C.; Neelakantan, P.; Chu, Z. Biofilm inhibition in oral pathogens by nanodiamonds. *Biomater. Sci.* **2021**, *9*, 5127–5135. [CrossRef] [PubMed]

37. Openda, Y.I.; Ngoy, B.P.; Nyokong, T. Photodynamic Antimicrobial Action of Asymmetrical Porphyrins Functionalized Silver-Detonation Nanodiamonds Nanoplatforms for the Suppression of Staphylococcus aureus Planktonic Cells and Biofilms. *Front. Chem.* **2021**, *9*. [CrossRef] [PubMed]

38. Openda, Y.I.; Nyokong, T. Detonation nanodiamonds-phthalocyanine photosensitizers with enhanced photophysicochemical properties and effective photoantibacterial activity. *Photodiagn. Photodyn. Ther.* **2020**, *32*, 102072. [CrossRef]

39. Yang, Y.; Chen, J.; Mao, Z.; An, N.; Wang, D.; Fahlman, B.D. Ultrathin g-C$_3$N$_4$ nanosheets with an extended visible-light-responsive range for significant enhancement of photocatalysis. *RSC Adv.* **2017**, *7*, 2333–2341. [CrossRef]

40. Zheng, Y.; Zhang, Z.; Li, C. A comparison of graphitic carbon nitrides synthesized from different precursors through pyrolysis. mboxemph*J. Photochem. Photobiol. A Chem.* **2017**, *332*, 32–44. [CrossRef]

41. Gomes, L.E.; da Silva, M.F.; Gonçalves, R.V.; Machado, G.; Alcantara, G.B.; Caires, A.R.L.; Wender, H. Synthesis and Visible-Light-Driven Photocatalytic Activity of Ta$_4$+ Self-Doped Gray Ta$_2$O$_5$ Nanoparticles. *J. Phys. Chem. C* **2018**, *122*, 6014–6025. [CrossRef]

42. Gomes, L.E.; Nogueira, A.C.; da Silva, M.F.; Plaça, L.F.; Maia, L.J.Q.; Gonçalves, R.V.; Ullah, S.; Khan, S.; Wender, H. Enhanced photocatalytic activity of BiVO$_4$/Pt/PtOx photocatalyst: The role of Pt oxidation state. *Appl. Surf. Sci.* **2021**, *567*, 150773. [CrossRef]

43. Li, K.; Gao, S.; Wang, Q.; Xu, H.; Wang, Z.; Huang, B.; Dai, Y.; Lu, J. In-Situ-Reduced Synthesis of Ti$_3$+ Self-Doped TiO$_2$/g-C3N$_4$ Heterojunctions with High Photocatalytic Performance under LED Light Irradiation. *ACS Appl. Mater. Interfaces* **2015**, *7*, 9023–9030. [CrossRef] [PubMed]

44. Ismael, M.; Wu, Y.; Taffa, D.H.; Bottke, P.; Wark, M. Graphitic carbon nitride synthesized by simple pyrolysis: Role of precursor in photocatalytic hydrogen production. *New J. Chem.* **2019**, *43*, 6909–6920. [CrossRef]

45. Piña-Salazar, E.-Z.; Kukobat, R.; Futamura, R.; Hayashi, T.; Toshio, S.; Ōsawa, E.; Kaneko, K. Water-selective adsorption sites on detonation nanodiamonds. *Carbon* **2018**, *139*, 853–860. [CrossRef]

46. Ishida, N.; Kato, K.; Suzuki, N.; Fujimoto, K.; Hagio, T.; Ichino, R.; Kondo, T.; Yuasa, M.; Uetsuka, H.; Fujishima, A.; et al. Preparation of amino group functionalized diamond using photocatalyst and thermal conductivity of diamond/copper composite by electroplating. *Diam. Relat. Mater.* **2021**, *118*, 108509. [CrossRef]

47. Gao, J.; Zhou, Y.; Li, Z.; Yan, S.; Wang, N.; Zou, Z. High-yield synthesis of millimetre-long, semiconducting carbon nitride nanotubes with intense photoluminescence emission and reproducible photoconductivity. *Nanoscale* **2012**, *4*, 3687–3692. [CrossRef]

48. Wang, X.; Maeda, K.; Thomas, A.; Takanabe, K.; Xin, G.; Carlsson, J.M.; Domen, K.; Antonietti, M. A metal-free polymeric photocatalyst for hydrogen production from water under visible light. *Nat. Mater.* **2008**, *8*, 76–80. [CrossRef]

49. Pina-Salazar, E.-Z.; Urita, K.; Hayashi, T.; Futamura, R.; Vallejos-Burgos, F.; Włoch, J.; Kowalczyk, P.; Wiśniewski, M.; Sakai, T.; Moriguchi, I.; et al. Water Adsorption Property of Hierarchically Nanoporous Detonation Nanodiamonds. *Langmuir* **2017**, *33*, 11180–11188. [CrossRef]

50. Xiang, Q.; Yu, J.; Jaroniec, M. Preparation and Enhanced Visible-Light Photocatalytic H$_2$-Production Activity of Graphene/C$_3$N$_4$ Composites. *J. Phys. Chem. C* **2011**, *115*, 7355–7363. [CrossRef]

51. Nunn, N.; Torelli, M.; McGuire, G.; Shenderova, O. Nanodiamond: A high impact nanomaterial. *Curr. Opin. Solid State Mater. Sci.* **2017**, *21*, 1–9. [CrossRef]

52. Aharonovich, I.; Greentree, A.D.; Prawer, S. Diamond photonics. *Nat. Photonics* **2011**, *5*, 397–405. [CrossRef]

53. Hertkorn, J.; Fyta, M. Electronic features of vacancy, nitrogen, and phosphorus defects in nanodiamonds. *Electron. Struct.* **2019**, *1*, 025002. [CrossRef]

54. Li, J.; Yin, Y.; Liu, E.; Ma, Y.; Wan, J.; Fan, J.; Hu, X. In situ growing Bi$_2$MoO$_6$ on g-C$_3$N$_4$ nanosheets with enhanced photocatalytic hydrogen evolution and disinfection of bacteria under visible light irradiation. *J. Hazard. Mater.* **2017**, *321*, 183–192. [CrossRef] [PubMed]

55. Li, G.; Nie, X.; Chen, J.; Jiang, Q.; An, T.; Wong, P.K.; Zhang, H.; Zhao, H.; Yamashita, H. Enhanced visible-light-driven photocatalytic inactivation of Escherichia coli using g-C$_3$N$_4$/TiO$_2$ hybrid photocatalyst synthesized using a hydrothermal-calcination approach. *Water Res.* **2015**, *86*, 17–24. [CrossRef]

56. Tan, H.L.; Wen, X.; Amal, R.; Ng, Y.H. BiVO$_4$ {010} and {110} Relative Exposure Extent: Governing Factor of Surface Charge Population and Photocatalytic Activity. *J. Phys. Chem. Lett.* **2016**, *7*, 1400–1405. [CrossRef]

57. Klimov, V.; Bolívar, P.H.; Kurz, H. Ultrafast carrier dynamics in semiconductor quantum dots. *Phys. Rev. B* **1996**, *53*, 1463–1467. [CrossRef] [PubMed]

58. Lin, X.; Hou, J.; Jiang, S.; Lin, Z.; Wang, M.; Che, G. A Z-scheme visible-light-driven Ag/Ag$_3$PO$_4$/Bi$_2$MoO$_6$ photocatalyst: Synthesis and enhanced photocatalytic activity. *RSC Adv.* **2015**, *5*, 104815–104821. [CrossRef]

59. Zhang, L.; Dai, Z.; Zheng, G.; Yao, Z.; Mu, J. Superior visible light photocatalytic performance of reticular BiVO$_4$ synthesized via a modified sol–gel method. *RSC Adv.* **2018**, *8*, 10654–10664. [CrossRef]

60. Geng, Y.; Zhang, P.; Li, N.; Sun, Z. Synthesis of Co doped BiVO$_4$ with enhanced visible-light photocatalytic activities. *J. Alloys Compd.* **2015**, *651*, 744–748. [CrossRef]

61. Su, L.-X.; Liu, Z.-Y.; Ye, Y.-L.; Shen, C.-L.; Lou, Q.; Shan, C.-X. Heterostructured boron doped nanodiamonds@g-C3N4 nanocomposites with enhanced photocatalytic capability under visible light irradiation. *Int. J. Hydrogen Energy* **2019**, *44*, 19805–19815. [CrossRef]

62. Yuan, Y.; Zhang, L.; Xing, J.; Utama, M.I.B.; Lu, X.; Du, K.; Li, Y.; Hu, X.; Wang, S.; Genç, A.; et al. High-yield synthesis and optical properties of g-C$_3$N. *Nanoscale* **2015**, *7*, 12343–12350. [CrossRef] [PubMed]

63. Das, D.; Shinde, S.L.; Nanda, K.K. Temperature-Dependent Photoluminescence of g-C$_3$N$_4$: Implication for Temperature Sensing. *ACS Appl. Mater. Interfaces* **2016**, *8*, 2181–2186. [CrossRef] [PubMed]

64. Zhang, W.; Li, R.; Zhao, X.; Chen, Z.; Law, W.K.A.; Zhou, K. A Cobalt-Based Metal–Organic Framework as Cocatalyst on BiVO 4 Photoanode for Enhanced Photoelectrochemical Water Oxidation. *ChemSusChem* **2018**, *11*, 2710–2716. [CrossRef] [PubMed]

65. Liu, C.; Luo, H.; Xu, Y.; Wang, W.; Liang, Q.; Mitsuzaki, N.; Chen, Z. Cobalt–phosphate-modified Mo:BiVO$_4$ mesoporous photoelectrodes for enhanced photoelectrochemical water splitting. *J. Mater. Sci.* **2019**, *54*, 10670–10683. [CrossRef]

66. Ullah, S.; Fayeza; Khan, A.A.; Jan, A.; Aain, S.Q.; Neto, E.P.; Serge-Correales, Y.E.; Parveen, R.; Wender, H.; Rodrigues-Filho, U.P.; et al. Enhanced photoactivity of BiVO$_4$/Ag/Ag$_2$O Z-scheme photocatalyst for efficient environmental remediation under natural sunlight and low-cost LED illumination. *Colloids Surfaces A Physicochem. Eng. Asp.* **2020**, *600*, 124946. [CrossRef]